Composite Structures 325 (2023) 117612

Contents lists available at ScienceDirect

Composite Structures

journal homepage: www.elsevier.com/locate/compstruct

Characterization of wave propagation in complex composite structures (CCS) using a robust inverse analysis method

Xuefeng Li [a], Mohamed Ichchou [a,*], Pascal Fossat [a], Abdelmalek Zine [b], Noureddine Bouhaddi [c]

[a] École Centrale de Lyon, Vibroacoustics & Complex Media Research Group, LTDS - CNRS UMR 5513, Écully 69134, France
[b] École Centrale de Lyon, Institut Camille Jordan - CNRS UMR 5208, Écully, France
[c] Univ. Bourgogne Franche-Comté, FEMTO-ST Institute, Department of Applied Mechanics, CNRS/UFC/ENSMM/UTBM, Besançon, France

ARTICLE INFO

Keywords:
Honeycomb sandwich structures
Locally resonant composite structures
Rib-stiffened composite structures
Wavenumber extraction
Wave propagation characterization
Inverse identification

ABSTRACT

This paper presents the application of wave propagation characterization for complex composite structures through the Algebraic K-space Identification technique in the Cartesian coordinate system (AKSI-C). The proposed method is a novel development since the developed methodology uses adequate partial differential algebraic operations to provide a robust and low-cost framework for identifying wave propagation parameters of the structures with multidimensional signals for the first time. Additionally, the proposed method has been experimentally applied to identify the complex wave propagation phenomenon of different complex composite structures: (i) honeycomb sandwich composite structure: variability of orthotropic behavior and damping properties with frequency and direction is identified by wavenumber space, 3D dispersion curves, and damping loss factor surface. Then, the contribution of individual layer properties on the changes in dynamic behavior is studied by estimating transition frequency; (ii) locally resonant meta-structure: the effect of the local resonator-induced band gap on the wave attenuation is investigated; (iii) periodic rib-stiffened composite plates: the inner resonance phenomena and their remarkable elastic wave manipulation ability are explored by designing 3D-printed resonators and identifying the mixed-resonance-induced band gap. The proposed method has been compared with other inverse methods to assess its reliability under complex conditions.

1. Introduction

Complex composite structures are widely used in aerospace engineering because of their special mechanical properties. A typical example of a complex composite structure is the honeycomb sandwich structure, which has a high strength-to-weight ratio. Such structures not only meet industrial requirements for weight reduction but also have damping properties and transmission capabilities [1,2]. In recent years, meta-structures have gained increasing interest due to their ability to generate band gaps where elastic waves cannot propagate along waveguides [3,4]. Another structure with the same properties is the periodically ribbed reinforced composite structures, which can also achieve a certain degree of balance between its surface rigidity and weight [5–7]. The performance of these structures can be improved by careful design and optimization. However, the design and optimization of these structures in a vibroacoustic environment remain challenging as the realization of this process is closely linked to the accurate prediction of the dynamic behavior of the structures and the identification of the mechanical parameters.

To describe the dynamic behavior of composite structures, although a large number of numerical methods [8–11] are available in the literature, the geometrical complexity of complex composite structures yields a challenge for numerical modeling in terms of accuracy and computational cost. In addition, the analytical or semi-analytical [12–18] methods have poor performance at high frequencies due to the high modal density. Another limitation is that these traditional methods require that the mechanical parameters of the components of a complex composite structure are accurately known. However, the discrepancy between the mechanical parameters obtained from the static experiments (manufacturing process) and the real mechanical parameters inevitably results in the inaccuracy of these methods.

As alternatives, the inverse methods for experiment-based wave propagation parameter identification have attracted more and more attention in the vibroacoustic community in recent years [19–26]. The inverse methods require only the structural displacement field to be known. The whole process can be easily conducted in experimental tests by combining with scanning Doppler laser vibrometers, thereby significantly increasing their value for industrial applications. By analyzing the extracted wave propagation parameters, such as wavenumber space (k-space), dispersion relations, damping loss factors, and

* Correspondence to: École Centrale de Lyon, 36, Avenue Guy de Collongue, Écully 69134, France.
E-mail address: mohamed.ichchou@ec-lyon.fr (M. Ichchou).

https://doi.org/10.1016/j.compstruct.2023.117612
Received 20 July 2023; Received in revised form 16 September 2023; Accepted 7 October 2023
Available online 12 October 2023

band gaps, the dynamic behavior of structures and the physical properties of wave propagation can be fully described. Furthermore, these identified parameters can also be used for structural design and optimization. To actively modulate the capability of a structure in terms of structural vibration reduction, one strategy is to install 3D-printed local resonators on the surface of the structure, thereby stimulating the generation of band gaps. The position of the band gap or the frequency band of the wave attenuation can be regulated by tuning the number, mass, and distribution density of the local resonators. Claeys [27,28] has demonstrated the wave attenuation behavior induced by tunable resonators, and the Inhomogeneous Wave Correlation (IWC) method was applied to study the ability of locally resonant meta-structure on vibration control in [6,29]. In addition, the ribs-stiffened plate is a special kind of composite structure. Coupled stiffener and plate behavior is capable of inducing inner resonance phenomena. By adjusting the coupling relationship between the stiffeners and the plate, the high tunability of the band gap can be achieved for vibration energy manipulation. The multi-mode wave propagation characterization and coupled dynamic behavior of such structures were studied using IWC in [5,30]. In [31], IWC was also applied to estimate the dynamic structural properties of a honeycomb sandwich structure using the extracted k-space, which is beneficial for the optimization of the layered composite structure. The widespread use of IWC is due to its high robustness against perturbations. However, IWC suffers from the low-frequency limitation and the high computational cost [24,25]. The Fast Fourier Transform (FFT) is a widely used inverse method to extract parameters of signal with a low computational cost. The 3D-FFT was used to extract the wavenumbers of three different composite plates in [32]. However, the main limitation of the FFT-based method is that it suffers from low frequencies and can only extract the real part of wavenumbers. In [33], authors used a classic linear inverse method, the Matrix Pencil (MP) method, to extract the dispersion curves of isotropic and anisotropic plates. This method requires periodic samples as input parameters. Another well-known low-cost linear inverse method is the Prony method, which has been applied to identify dispersion curves in a 5-layer red spruce plywood [34] and a constrained-layer damping sandwich plate [35]. Based on the principle of the Pony method, the High-Resolution Wavevector Analysis (HRWA) was proposed and applied to characterize the local elastic behavior of three composite structures and estimate the bending stiffness of a carbon-epoxy plate in [24]. Recently, the INverse COnvolution MEthod (INCOME) has been proposed in [25], which allows extracting a complete and accurate k-space in the noiseless environment. However, these methods suffer from the limitations of Prony's method: periodic sampling constraints and noise sensitivity.

To overcome the main limitations of IWC and Prony-based methods, an Algebraic Wavenumber Identification (AWI) technique was proposed in [36] to extract the wave propagation parameters of a one-dimensional periodic structure under stochastic conditions. This method is developed in a robust and low-cost algebraic parameter identification scheme [37]. AWI first establishes an ordinary differential equation (ODE) using the Laplace transform, and then a regression equation is established using the inverse Laplace transform, which contains multiple integrals of the signal. Finally, the wavenumber is extracted by estimating the unknown parameters of this ordinary differential equation. For two-dimensional signals, the identification of the partial differential equation (PDF) requires to be solved. Although the AWI can be extended to 2D signals in the polar coordinate system by the transformation of the coordinate systems, which is equivalent to the fact that PDE is transformed to ODE, the extension of AWI to 2D signals is worth investigating in the Cartesian coordinate system. This is because: (i) in the mechanical field, AWI needs to be fundamentally extended to identify wave propagation parameters of 2D and even multidimensional signals; (ii) the mathematical modeling in many areas can be represented as a PDE, and the reliable identification of the parameters of the PDE remains a central problem. Therefore, it is necessary to provide a reliable theoretical basis for parameter estimation of multivariate partial differential equations in the algebraic parameter identification scheme.

In this paper, the first purpose is to propose Algebraic K-Space Identification in the Cartesian coordinate system (AKSI-C), which is a robust and low-cost inverse method for wave propagation characterization of complex structures with 2D signals and even multidimensional signals. The main advantages of the proposed method are the robustness against signal noise, estimation of the resonators-related band gaps, freedom from the constraint of 2D periodic grid mesh, and low computational cost, which are experimentally validated by comparing with other inverse methods. The second objective of this paper is dedicated to the experimental characterization of wave propagation in four complex composite structures, including a honeycomb sandwich composite structure, a locally resonant meta-structure, and two periodic rib-stiffened composite plates. The main contributions of these applications are summarized as: (i) dynamic properties and wave propagation characteristics of the honeycomb sandwich structure, including variability of orthotropic dynamic behavior and damping properties, wave dispersion and energy propagation characteristics, the contribution of individual layer properties on changes in dynamic behavior, and transition frequency estimation are investigated by the extracted k-space, damping loss factor surface, and 3D dispersion curve; (ii) the effect of the tunability of the local resonator-related band gap on the wave attenuation is investigated by identifying the experimental dispersion curve of the locally resonant meta-structure; (iii) the inner resonance phenomena of the orthogonally ribbed plate and mixed-resonance-induced band gap of the uni-directionally ribbed plate are investigated, respectively.

The rest of this paper is organized as follows: Section 2 introduces the AKSI-C formulation and homogenized equation of the periodic rib-stiffened composite plate. Section 3 presents the experimental set-up and the tested structures. The experimental results and discussions are provided in Section 4. Finally, some conclusions are summarized in Section 5.

2. Methodology

This section focuses on introducing the theory of the proposed inverse method (Section 2.1), and the analytical method for calculating the flexural dispersion relation of the periodic rib-stiffened composite plate (Section 2.2).

2.1. Algebraic K-space identification in the Cartesian coordinate system (AKSI-C)

AKSI-C aims to extract the complex wavenumbers of 2D structures in each direction only using structural displacement. In the experimental environment, the harmonic displacement of a plate along a certain angle θ can be modeled by n_w plane waves and the additional signal noise as follows:

$$U(x,y)=\sum_{m=1}^{n_w}A_m e^{\mathrm{i}k_m(x\cos(\theta)+y\sin(\theta))}+b(x,y)=\sum_{m=1}^{n_w}A_m e^{\mathrm{i}k_{x,m}x}e^{\mathrm{i}k_{y,m}y}+b(x,y) \tag{1}$$

where n_w is the number of waves. $k_{x,m}$ and $k_{y,m}$ are the components of the wavenumber k_m of the 2D signal in the x direction and y direction. A_m is the complex amplitude. $b(x,y)$ is the additional noise part. To facilitate the derivation of the formula, the additional noise part is ignored at this moment. Therefore, the displacement at measuring point (x_n, y_n) along a certain angle θ can be expressed as follows:

$$U(x_n,y_n)=\sum_{m=1}^{n_w}A_m e^{h_m(x_n\cos(\theta)+y_n\sin(\theta))}=\sum_{m=1}^{n_w}A_m e^{p_m x_n}e^{q_m y_n} \tag{2}$$

where h_m, p_m and q_m are jk_m, $jk_{x,m}$, and $jk_{y,m}$, respectively. When applying the multivariate Laplace transform to Eq. (2), one can obtain the following equation in the wavenumber domain:

$$S(s_x, s_y) = \frac{A_1}{s_x - p_1}\frac{1}{s_y - q_1} + \frac{A_2}{s_x - p_2}\frac{1}{s_y - q_2} + \cdots + \frac{A_{n_w}}{s_x - p_{n_w}}\frac{1}{s_y - q_{n_w}} \quad (3)$$

Now, three characteristic polynomials related to $k_{x,m}$, $k_{y,m}$ and k_m in the wavenumber domain can be defined, respectively:

$$\Psi(s_x) = \prod_{m=1}^{n_w}(s_x - p_m) = \sum_{i=0}^{n_w}\gamma_x(n_w - i)s_x^i \quad (4)$$

$$\Psi(s_y) = \prod_{m=1}^{n_w}(s_y - q_m) = \sum_{i=0}^{n_w}\gamma_y(n_w - i)s_y^i \quad (5)$$

$$\Psi(s) = \prod_{m=1}^{n_w}(s - h_m) = \sum_{i=0}^{n_w}\gamma(n_w - i)s^i \quad (6)$$

where $\gamma_x(n_w - i)_{\{i\in[0,n_w]\}}$, $\gamma_y(n_w - i)_{\{i\in[0,n_w]\}}$ and $\gamma(n_w - i)_{\{i\in[0,n_w]\}}$ are unknown coefficients of three characteristic polynomials, respectively.

The first step of AKSI-C is to establish a partial differential equation. To this end, a new polynomial can first be obtained by multiplying Eqs. (3) and (4):

$$\begin{aligned} S(s_x, s_y)\Psi(s_x) &= \left(\frac{A_1}{s_x - p_1}\frac{1}{s_y - q_1} + \frac{A_2}{s_x - p_2}\frac{1}{s_y - q_2} + \cdots \right. \\ &\quad \left. + \frac{A_{n_w}}{s_x - p_{n_w}}\frac{1}{s_y - q_{n_w}}\right) \times \prod_{m=1}^{n_w}(s_x - p_m) \\ &= \sum_{m=1}^{n_w}\frac{A_m\prod_{i=1,i\neq m}^{n_w}(s_x - p_i)}{s_y - q_m} \end{aligned} \quad (7)$$

In the following context, we focus on the derivation of the formula about variable s_x for simplicity due to the fact that the same identification process is suitable for variable s_y. Clearly, Eq. (7) is a polynomial with the highest order of $n_w - 1$. Thus, a partial differential equation can be derived by taking partial derivatives n_w times with respect to s_x for Eq. (7):

$$\frac{\partial^{n_w}\left[S(s_x, s_y)\Psi(s_x)\right]}{\partial s_x^{n_w}} = \frac{\partial^{n_w}\left[S(s_x, s_y)\sum_{i=0}^{n_w}\gamma_x(n_w - i)s_x^i\right]}{\partial s_x^{n_w}} = 0 \quad (8)$$

To calculate Eq. (8), the following equations are introduced:

$$\frac{\partial^{n_w}\left[S(s_x, s_y)\Psi(s_x)\right]}{\partial s_x^{n_w}} = \sum_{j=0}^{n_w}\binom{n_w}{j}\frac{\partial^{n_w - j}(S(s_x, s_y))}{\partial s_x^{n_w - j}}\frac{\partial^j(\Psi(s_x))}{\partial s_x^j} \quad (9)$$

$$\frac{\partial^{n_w}(s_x^j)}{\partial s_x^{n_w}} = \frac{j!}{(j - n_w)!}s_x^{j - n_w} \quad (10)$$

After applying Eqs. (9) and (10) to the partial differential equation Eq. (8), we can easily obtain the following equation:

$$\sum_{i=0}^{n_w}\sum_{j=i}^{n_w}\binom{n_w}{j}\binom{n_w - i}{n_w - j}(n_w - j)!s_x^{j-i}\frac{\partial^j S(s_x, s_y)}{\partial s_x^j}\gamma_x(i) = 0 \quad (11)$$

The second step of AKSI-C is establishing an exact regression equation in the spatial domain. To achieve that, the division by $s_x^{n_w+1}$ is first applied to Eq. (11) as follows:

$$\sum_{i=0}^{n_w}\sum_{j=i}^{n_w}\binom{n_w}{j}\binom{n_w - i}{n_w - j}(n_w - j)!\frac{1}{s_x^{n_w+1+i-j}}\frac{\partial^j S(s_x, s_y)}{\partial s_x^j}\gamma_x(i) = 0 \quad (12)$$

Then, we apply the inverse Laplace transform to Eq. (12) to obtain the corresponding expression in the spatial domain. The multivariate inverse Laplace transform is introduced as follows:

$$\mathcal{L}^{-1}\left(\frac{1}{\boldsymbol{s}^{\boldsymbol{I}}}\frac{\partial^{\boldsymbol{J}}S(\boldsymbol{s})}{\partial\boldsymbol{s}^{\boldsymbol{J}}}\right) = \frac{1}{(\boldsymbol{I}-\boldsymbol{1})!}\int_{\boldsymbol{0}}^{\boldsymbol{X}}\upsilon_{\boldsymbol{I}-\boldsymbol{1},\boldsymbol{J}}(\boldsymbol{\tau})U(\boldsymbol{\tau})\,\mathrm{d}\boldsymbol{\tau} \quad (13)$$

with

$$\upsilon_{\boldsymbol{I},\boldsymbol{J}}(\boldsymbol{\tau}) = (\boldsymbol{X} - \boldsymbol{\tau})^{\boldsymbol{I}}(-\boldsymbol{\tau})^{\boldsymbol{J}} \quad (14)$$

where $\boldsymbol{I} = (I_1, \ldots, I_h)$ and $\boldsymbol{J} = (J_1, \ldots, J_h)$ are two multi-indices. $\boldsymbol{\tau} = (\tau_1, \ldots, \tau_h)$ and $\boldsymbol{1} = (1, \ldots, 1)$. $\boldsymbol{X} = (x_1, \ldots, x_h)$ and $\boldsymbol{s}^{\boldsymbol{I}} = s_1^{I_1}\ldots s_h^{I_h}$ are related to the multiple variables of the multivariate function U and its Laplace transform S. For the integral in Eq. (13), it is defined as:

$$\int_{\boldsymbol{0}}^{\boldsymbol{X}}U(\boldsymbol{\tau})\mathrm{d}\tau = \int_{\boldsymbol{0}}^{\boldsymbol{x_1}}\ldots\int_{\boldsymbol{0}}^{\boldsymbol{x_h}}U(\tau_1, \ldots, \tau_h)\,\mathrm{d}\tau_1\ldots\mathrm{d}\tau_h \quad (15)$$

It is easy to see that in Eq. (12), $h = 2$, $\boldsymbol{s}^{\boldsymbol{I}} = s_x^{n_w+1+j-i}$ and $\boldsymbol{J} = j$. In addition, $\boldsymbol{X}$ is (x_n, y_n), which is the coordinate of each measurement point of the 2D structures. Based on this, substituting Eq. (13) into Eq. (12) leads to the following equation:

$$\begin{aligned} &\sum_{i=0}^{n_w}\sum_{j=i}^{n_w}\binom{n_w}{j}\binom{n_w - i}{n_w - j}(n_w - j)!\frac{1}{(n_w + i - j)!} \\ &\quad\times\int_0^{x_n}\int_0^{y_n}(x_n - \tau_1)^{n_w+i-j}(-\tau_1)^j U(\tau_1, \tau_2)\,\mathrm{d}\tau_1\mathrm{d}\tau_2\;\gamma_x(i) = 0 \end{aligned} \quad (16)$$

For the simplicity, Eq. (16) can be written as:

$$\sum_{i=0}^{n_w}\phi(i, x_n, y_n)\gamma_x(i) = 0 \quad (17)$$

with

$$\begin{aligned} \phi(i, x_n, y_n) &= \sum_{j=i}^{n_w}\binom{n_w}{j}\binom{n_w - i}{n_w - j}(n_w - j)!\frac{1}{(n_w + j - i)!} \\ &\quad\times\int_0^{x_n}\int_0^{y_n}(x_n - \tau_1)^{n_w+i-j}(-\tau_1)^j U(\tau_1, \tau_2)\,\mathrm{d}\tau_1\mathrm{d}\tau_2 \end{aligned} \quad (18)$$

where the integrals can also be calculated by means of numerical integration, such as the trapezoidal integration method.

The third step of AKSI-C is to estimate $\gamma_x(i)$ of Eq. (17) using the least-squares method. Since Eq. (17) holds for each measurement point, one can take its matrix format as follows:

$$\mathbf{H_x}\mathbf{X_x} = \mathbf{M} \quad (19)$$

with

$$\mathbf{H_x} = \begin{bmatrix} \phi(n_w, x_1, y_1) & \phi(n_w - 1, x_1, y_1) & \cdots & \phi(0, x_1, y_1) \\ \phi(n_w, x_2, y_2) & \phi(n_w - 1, x_2, y_2) & \cdots & \phi(0, x_2, y_2) \\ \vdots & \vdots & \ddots & \vdots \\ \phi(n_w, x_N, y_N) & \phi(n_w - 1, x_N, y_N) & \cdots & \phi(0, x_N, y_N) \end{bmatrix},$$

$$\mathbf{X_x} = \begin{bmatrix} \gamma_x(n_w) \\ \gamma_x(n_w - 1) \\ \vdots \\ \gamma_x(0) \end{bmatrix}, \qquad \mathbf{M} = \begin{bmatrix} 0 \\ 0 \\ \vdots \\ 0 \end{bmatrix} \quad (20)$$

where $\mathbf{X_x}$ is the eigenvector corresponding to the smallest eigenvalue of $\mathbf{H_x^*H_x}$.

The final step of AKSI-C is to estimate wavenumber k_m from the estimated $\gamma_x(i)$, which are the coefficients of Eq. (4). One of the strategies is first to calculate coefficients $\gamma(i)$ of Eq. (6) by the estimated $\gamma_x(i)$. Then the wavenumber k_m can be directly obtained by calculating the roots of Eq. (6). To this end, it is necessary to conduct adequate algebraic manipulations on Eq. (4) to establish a relationship between $\gamma_x(i)$ and $\gamma(i)$. It is obvious that Eq. (4) is a monic univariate polynomial, which can be extended as follows:

$$\begin{aligned} \Psi(s_x) &= \prod_{m=1}^{n_w}(s_x - p_m) = \sum_{i=0}^{n_w}\gamma_x(n_w - i)s_x^i \\ &= \gamma_x(n_w) + \gamma_x(n_w - 1)s_x + \cdots + \gamma_x(1)s_x^{n_w - 1} + \gamma_x(0)s_x^{n_w} \end{aligned} \quad (21)$$

In the field of algebra, Vieta's formulas and the Galois theory provide an essential conclusion: coefficients of a monic univariate polynomial of degree n with n roots are the symmetric polynomial functions of the roots. On this basis, the coefficients of Eq. (21) can be represented as:

$$\gamma_x(n_w - i) = (-1)^{n_w - i}\sum_{1\le j_1<j_2<\cdots<j_{n_w-i}\le n_w}p_{j_1}p_{j_2}\cdots p_{j_{n_w-i}}$$

$$= (-1)^{n_w-i} \sum_{1\le j_1<j_2<\cdots<j_{n_w-i}\le n_w} \mathrm{j}k_{x,j_1}\mathrm{j}k_{x,j_2}\cdots\mathrm{j}k_{x,j_{n_w-i}} \tag{22}$$

where $\gamma_x(n_w-i)$ is expressed in the format of symmetric polynomial. It is well known that wavenumber k_m and its components $k_{x,m}$ have the following relationship:

$$k_{x,m} = k_m\cos(\theta), \qquad n = 1,\ldots,N \tag{23}$$

Therefore, one can obtain the following equation after substituting Eq. (23) into Eq. (22):

$$\begin{aligned}\frac{\gamma_x(n_w-i)}{(\cos(\theta))^{n_w-i}} &= (-1)^{n_w-i} \sum_{1\le j_1<j_2<\cdots<j_{n_w-i}\le n_w} \frac{\mathrm{j}k_{x,j_1}}{\cos(\theta)}\frac{\mathrm{j}k_{x,j_2}}{\cos(\theta)}\cdots\frac{\mathrm{j}k_{x,j_{n_w-i}}}{\cos(\theta)} \\ &= (-1)^{n_w-i} \sum_{1\le j_1<j_2<\cdots<j_{n_w-i}\le n_w} \mathrm{j}k_{j_1}\mathrm{j}k_{j_2}\cdots\mathrm{j}k_{j_{n_w-i}}\end{aligned} \tag{24}$$

It is worth noting that Eq. (24) is the expression of coefficients of Eq. (6). Therefore, the $\gamma(i)$ can be obtained by the following relationship:

$$\gamma(n_w-i) = \frac{\gamma_x(n_w-i)}{(\cos(\theta))^{n_w-i}} \tag{25}$$

Once $\gamma(n_w-i)_{\{i\in[0,n_w]\}}$ are obtained, the k_m can be extracted by $k_m = \mathrm{j}h_m$ where h_m are the roots of Eq. (6). Based on the extracted complex wavenumbers k_m, the damping loss factor can be estimated by the following equation [38,39]:

$$\eta = \left|\frac{\mathrm{Im}(k_m^4)}{\mathrm{Re}(k_m^4)}\right| \tag{26}$$

Three particular emphases are put on the formulation of AKSI-C: (i) the integral of signal in spatial domain act as a filter, reducing the influence of signal noise; (ii) AKSI-C treats the signal as a continuous function, free from periodic sampling; (iii) the AKSI-C only requires solving several linear equations, having a low computational cost.

Two main innovations of the AKSI-C in relation to the AWI are worth providing:

- From the methodology point of view, AKSI-C improves AWI essentially to extract wavenumbers of composite plates by using the multivariate Laplace transforms and inverse Laplace transforms to process partial differential equation Eq. (11) with two unknown parameters k_x and k_y. However, the essence of AWI is the estimation of unknown coefficients of the ordinary differential equation having only one unknown parameter k. AKSI-C can be easily extended to the complex wavenumbers identification of multidimensional signals due to the application of multivariate inverse Laplace transform, in which Eq. (18) requires the calculation of multidimensional integration. This makes it possible to apply AKSI-C to more complex structures, such as 3D cubic or curved structures. AKSI-C provides a fast and robust framework for parameter estimation of partial differential equations, opening up the possibility of extending the method to more complex problems, such as material identification of analytical models.
- From the practical application point of view, compared to a 1D structure, the wave field of a low-damping plate is complicated by the fact that it is subject to the superposition of multiple propagating and reflected waves. The model order estimation (estimation of the number of waves) becomes important. To this end, two widely used methods, Maximum Description Length (MDL) [40] and ESTimation of ERror (ESTER) [41], can be applied to estimate the number of waves. The reader is referred to [23,42], where these two well-established methods were also successfully applied to estimate the number of waves of plates, respectively.

To successfully apply AKSI-C to extract wave propagation parameters for real materials in an experimental environment, three measurement strategies adapted to AKSI-C are summarized from experiment tests: (1) the use of the samples in the shorter line mesh satisfying Shannon's theorems is suggested as input parameters because the model order estimation method performs well for a reduced model order; (2) the smaller sampling interval is suggested to be used when signal noise is high, this is because that the numerical precision of numerical integration calculated in Eq. (18) increase with increasing nodes in the integration interval, enhancing the robustness of AKSI-C to signal noise; (3) the measurement samples located at the location far away from force source and boundary condition are recommended to be chosen as input parameters to reduce the influence of evanescent wave on the extracted wavenumber.

2.2. Homogenized equation of the periodic rib-stiffened composite plate

The periodic rib-stiffened composite plate studied in the present work includes a uni-directionally ribbed plate and an orthogonally ribbed plate. In this section, the latter is taken as an example to illustrate a homogenized analytical model to describe the dynamic behavior of such structures. Fig. 1(a) shows the model of the orthogonally ribbed plate, which consists of an internal plate clamped by stiffeners (beam grids) in the x and y directions. The periodically spaced beam grid is assumed to be stiffer than the inner plate, controlling the dynamics of the structures. The geometric parameters are shown in the unit cell in Fig. 1(b), where l_j, b_j, and h_j $(j = x, y)$ are the length, width, and thickness of the beam grid in two directions. The d is the thickness of the internal plate. Based on this model, a 4th-order homogenized equation to calculate the analytical bending dispersion relation of the ribbed plate is proposed in [5]:

$$\begin{aligned}&k_m^4\left(\frac{E_xI_x}{l_x}\cos^4(\theta)+\frac{E_yI_y}{l_y}\sin^4(\theta)+\left(\frac{G_x\mathcal{I}_x}{l_y}+\frac{G_y\mathcal{I}_y}{l_x}\right)\cos^2(\theta)\sin^2(\theta)\right) \\ &\quad-\omega^2\left(\frac{\Lambda_x}{l_y}+\frac{\Lambda_y}{l_x}+\Lambda_p'\left\langle\varphi_\omega^{ribbed}\right\rangle\right)=0\end{aligned} \tag{27}$$

with

$$\begin{aligned}I_j &= \frac{b_jh_j^3}{12}, \qquad \Lambda_j = \rho_jb_jh_j, \\ \mathcal{I}_j &= \frac{b_j}{2}\left(\frac{h_j}{2}\right)^3\left(\frac{16}{3}-3.36\frac{h_j}{b_j}\left(1-\frac{h_j^4}{12b_j^4}\right)\right), \qquad \Lambda_p' = \rho_pd\end{aligned} \tag{28}$$

where $\rho_j, E_j, G_j, I_j, \Lambda_j$, and $\mathcal{I}_j$ $(j = x, y)$ are the volume mass, Young modulus, torsional modulus, bending inertia, linear mass and the torsional inertia for beam grids in two directions, ρ_p and Λ_p' are the volume mass and the surface mass of the internal plate. $\left\langle\varphi_\omega^{ribbed}\right\rangle$ reflects the inner resonance phenomena of the ribbed plate, leading to the occurrence of the band gap in the dispersion curve. This factor is determined by the type of ribbed plate, and in this paper, the corresponding results to the unidirectional ribbed plate and the orthogonal ribbed plate are:

$$\left\langle\varphi_\omega^{ribbed_{uni}}\right\rangle = \frac{2}{\delta l_x}\frac{1}{\coth(\delta l_x)+\cot(\delta l_x)} \tag{29}$$

$$\left\langle\varphi_\omega^{ribbed_{orth}}\right\rangle = \frac{4}{\delta a}\left(\frac{J_0(\delta a)}{J_1(\delta a)}+\frac{I_0(\delta a)}{I_1(\delta a)}\right)^{-1}, \qquad a\approx 0.53l_x \tag{30}$$

where $\delta = \sqrt[4]{(\Lambda_p'\omega^2)/(E_p'I_p')}$ with plate modulus $E_p' = E_p/(1-\upsilon_p^2)$, bending inertia $I_p' = d^3/12$, and bending modulus E_p of the internal plate. J_0 and J_1 are the Bessel function of the first kind, while I_0 and I_1 are the modified ones.

3. Experimental tests

In this section, three types of complex composite structures are experimentally tested, including a honeycomb sandwich composite structure, a locally resonant meta-structure, and two periodic rib-stiffened composite plates. The experimental setup is shown in Section 3.1, and tested structures and measurements are introduced in Section 3.2.

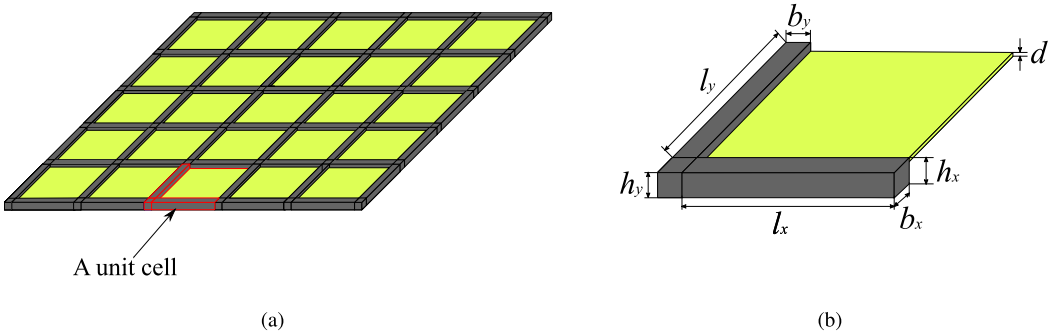

Fig. 1. (a) Orthogonally ribbed plate model with 5 × 5 unit cells. (b) Unit cell consisting of beam grids and an internal plate, and the notations related to the dimensions.

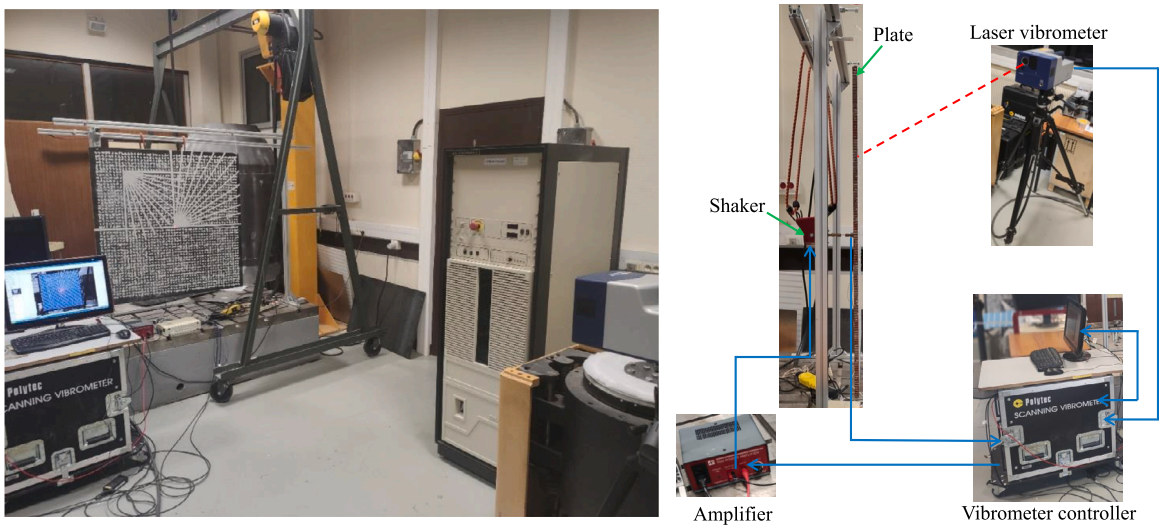

Fig. 2. Global view of the experimental setup for measuring transversal displacement field of tested complex composite structures.

3.1. Experimental setup

The full-field vibration measurement of the tested structures is conducted by scanning laser Doppler vibrometer (SLDV). The experimental setup is shown in Fig. 2. The structures are suspended in a fixed frame by Polylactic Acid filaments and excited by a point mechanical force using an electrodynamic shaker (Brüel & kJær, 4810). The structures and shaker are connected by a force sensor (Brüel & Kjaer type 8001) linked to the vibrometer controller. The out-of-plane displacement fields of structures are measured by a Polytec Scanning Vibrometer (PSV-400). Finally, the displacement fields are acquired by a Fourier analyzer connected with a sampler. The relationship of each part of the experimental setup is illustrated in Fig. 2.

3.2. Tested structures and data acquisition

In this paper, the AKSI-C is validated experimentally by comparing it with INCOME and IWC. Two different sampling ways are applied to satisfy the measurement characteristics of each inverse method: (i) measuring samples are measured along lines (AKSI-C and IWC); (ii) measuring samples are measured in a 2D regular grid (INCOME and IWC). The IWC can be compared with other inverse methods in each test because it is suitable for both sampling ways. The following subsections present tested structures and measurements in detail, respectively.

3.2.1. Honeycomb sandwich composite structure

The honeycomb sandwich composite structure studied in this work is shown in Fig. 3(a). This 1 m × 1 m structure is made of a 13 mm-thick light honeycomb core and two 0.5 mm-thick stiff skins oriented at 0° (see Fig. 3(c)). The material of the core is the Nida NOMEX, while the skin is made of carbon fiber epoxy (Hexcel reference 43199) with a 50% resin fiber ratio. The equivalent mechanical properties of this composite plate have been tested in [43] (See Table 1):

The line and 2D grid mesh are presented in Fig. 3(a) and Fig. 3(b), where the red points are excitation locations. For line mesh, the measurements were first carried out along thirteen radial directions between 0° and 90° with an angle step of 7.5° when the excitation position was at the center of the plate (point A in Fig. 3(a)). The positive x-axis and y-axis are seen as 0° and 90°, while the negative x-axis and y-axis are assumed as 180° and 270°. Then the same measuring process was conducted between 270° and 360° when the shaker was put in the corner of the plate (point B in Fig. 3(a)). In each radial direction, 59 equally spaced measurement points with a sampling interval of 0.37 cm are measured. For 2D mesh, the measurements were performed on a 49 × 49 grid with the 1.9 cm sampling interval along the x and y directions.

3.2.2. Locally resonant meta-structure

The locally resonant meta-structure is formed by adding small-scaled resonators on the surface of the host plate, as shown in Fig. 4(a). The host plate is a 0.95 m × 0.6 m steel plate with the thickness of 2 mm (E = 210 GPa, ν = 0.33, ρ = 7850 kg/m^3) and 65 uniform distributed resonators were mounted on the steel plate. The schematic representation of the resonator is shown in Fig. 4(d). The resonator is made of polycarbonate polymer by 3D printing technology, and its weight without a tuning mass is 2 g. From this figure, it can be seen that the resonator resembles a cantilever beam in its shape: a beam supported by a stiffener is connected to a base. In addition, a 1 g

Table 1
Equivalent mechanical properties of the honeycomb sandwich composite plate.

G_{xz} (MPa)	G_{yz} (MPa)	E_x (GPa)	Shear rigidity S (MPa)	Bending stiffness D (N·m)	Mass per unit area ρ (kg/m^2)
30	40	141	0.532	6420	1930

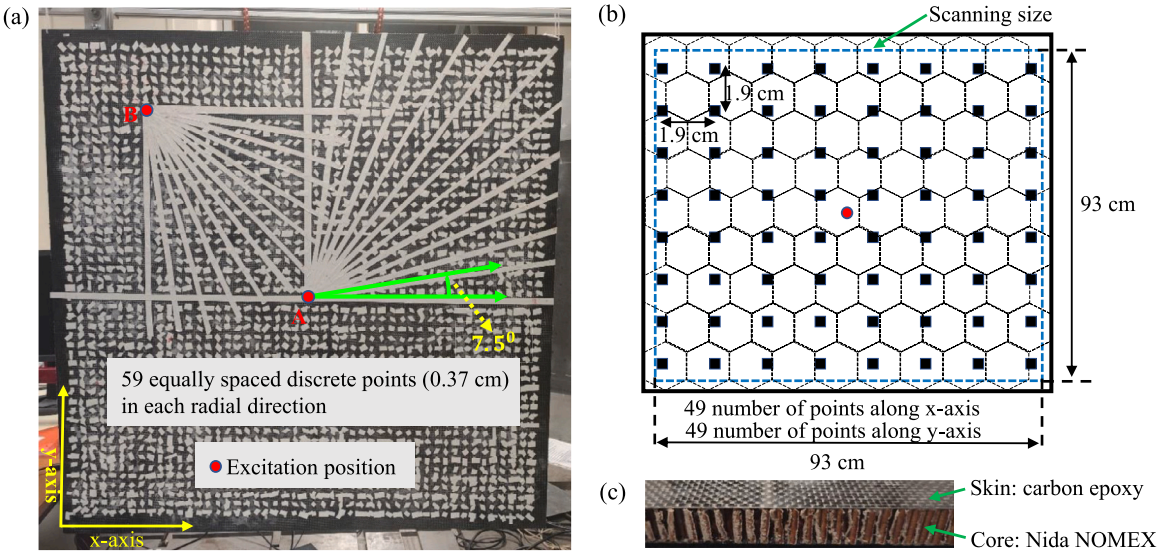

Fig. 3. Honeycomb sandwich composite plate: (a) line measurements along 26 radial directions; (b) 2D regularly spaced measurements mesh grid; (c) a section of the sandwich plate along the thickness.

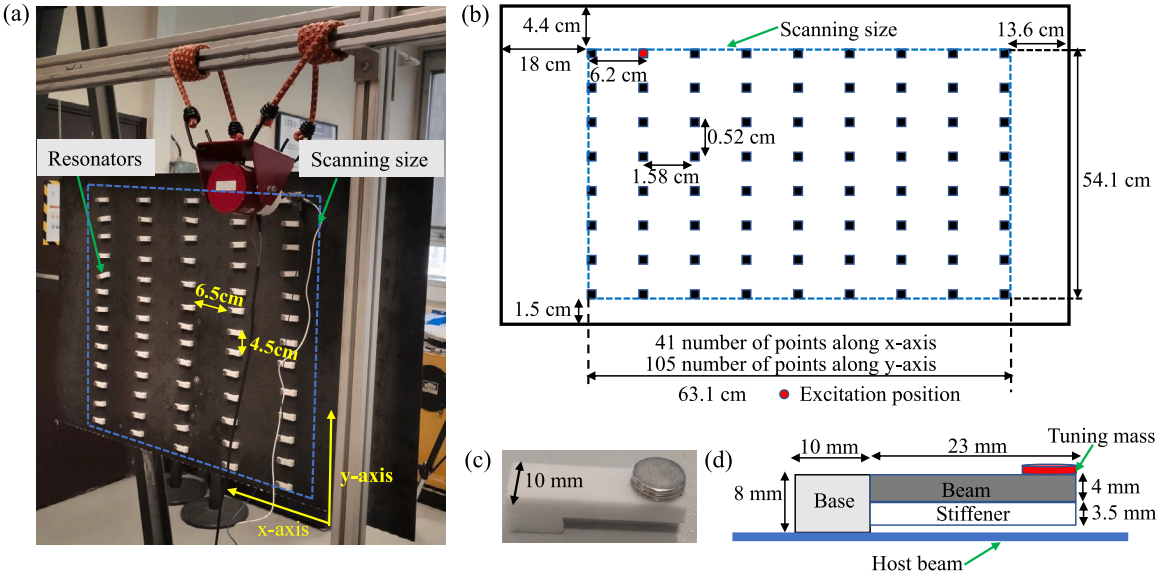

Fig. 4. Locally resonant meta-structure: (a) the steel plate with uniformly distributed small-scale resonators; (b) 2D regularly spaced measurements mesh grid; (c) the picture of a resonator with 3 g of the magnet; (d) schematic of the 3D printed resonator.

magnet is glued to the opposite side of the resonator. The weight of the resonator is tunable by increasing or decreasing the number of magnets, resulting in the adjustment of resonator frequency, which provides the possibility to control the wave attenuation in the frequency range of interest through the design of the resonators. The conception of this resonator and its capability to generate the band gap is illustrated in [44]. In this study, the weight of a resonator is adjusted to be 5 g by adding three magnets, as shown in Fig. 4(c). The corresponding resonator frequency is tuned to be 1284 Hz. The detailed information on 2D measurement mesh and excitation location are presented in Fig. 4(b).

3.2.3. Periodic rib-stiffened composite plates

Two types of ribbed plates in different configurations have been experimentally tested. Their characteristics are described as follows:

- Uni-directionally ribbed plate. This structure is made of an aluminum plate ribbed with 8 aluminum stiffeners spaced 90 mm apart. The internal plate has a dimension of 750 × 600 × 1 mm, and the stiffener has a size of 600 × 10 × 5 mm (see Fig. 5(a)). This ribbed plate in resonator configuration is also studied (see Fig. 5(b)).
- Orthogonally ribbed plate. This structure comprises a perspex (PMMA) plate ribbed with 12 aluminum stiffeners spaced 100 mm apart. The plate has a dimension of 560 × 560 × 1 mm, and the

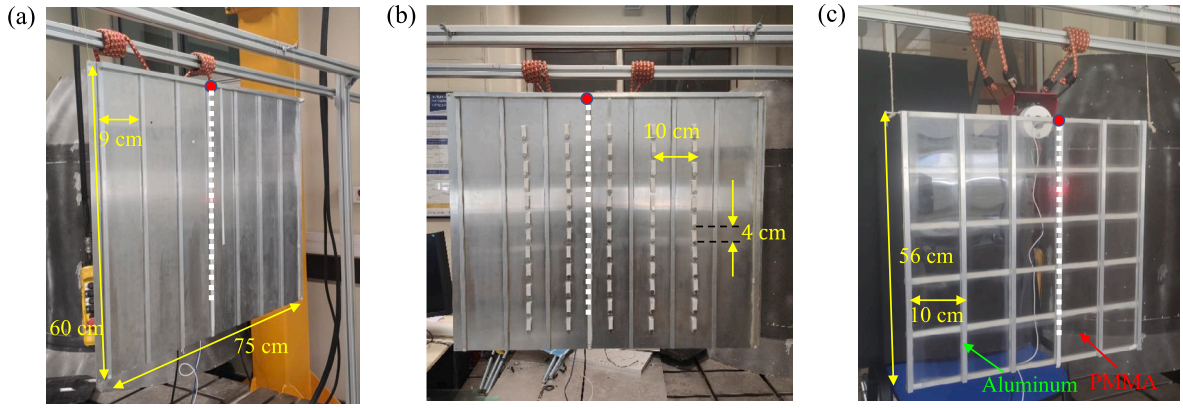

Fig. 5. Periodic rib-stiffened composite plates: (a) uni-directionally ribbed plate; (b) uni-directionally ribbed plate with resonators; (c) orthogonally ribbed plate.

Table 2
Geometrical and mechanical parameters of the orthogonally ribbed plate.

Material	Dimensions (mm)	Young Modulus (GPa)	Density (kg/m^3)	Weight (kg)
Stiffeners/ beam grids (Aluminum)	$h_x = h_y = b_y = b_x = 10$	69	2700	1.78
Plate (PMMP)	$l_x = l_y = 100, d = 1$	3	1200	0.363

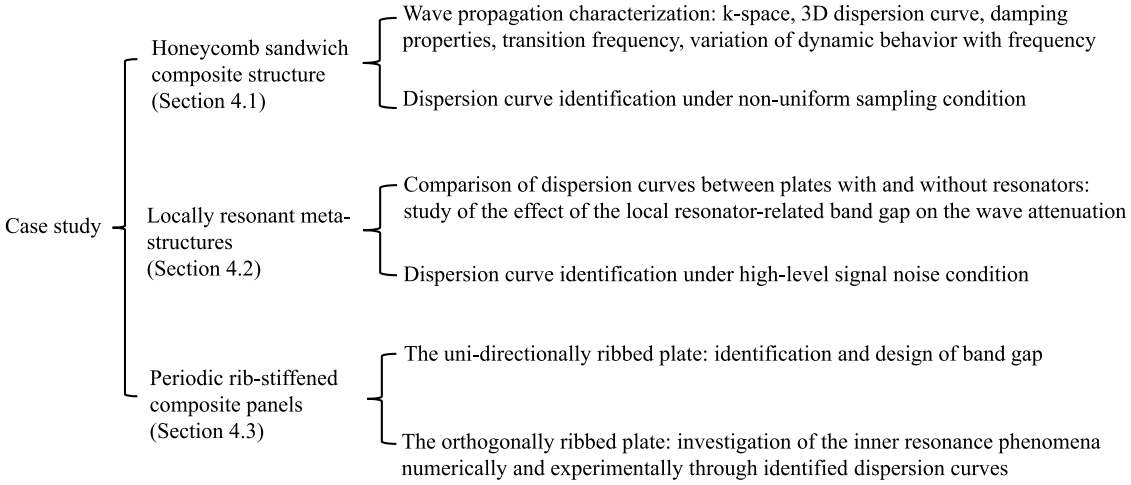

Fig. 6. Tree diagram of the case study.

stiffener has a size of 560 × 10 × 10 mm, generating 25 internal plates (100 × 100 mm) (see Fig. 5(c)).

In Fig. 5(b), 60 resonators are periodically distributed on the surface of the uni-directionally ribbed plate. The weight of a resonator is tuned to be 3 g. 100 equally spaced measuring points with a sampling interval of 0.4 cm along the line mesh (white dotted line shown in Fig. 5(b)) are measured in this test. For the orthogonally ribbed plate, 90 equally spaced samples with a sampling interval of 0.43 cm are considered. Its numerical model is shown in Fig. 1. The geometric and mechanical parameters are listed in Table 2. In order to eliminate the effect of evanescent waves on wavenumber extraction, the samples closed to the excitation and boundary condition are required to be removed. For this reason, the measurement samples with the exclusion of 50 points (lying closest to the ends of the plate, 25 points for each end) are used as input for the tested ribbed plates.

4. Results and discussions

In this section, the experimental results are presented and discussed. To clearly illustrate the purpose of each experimental study, we provide a tree diagram in the Fig. 6.

4.1. Honeycomb sandwich composite structure: Experimental results and validation

The dispersion curves in two principal directions extracted by AKSI-C are shown in Fig. 7(a), which has a good agreement with the analytical dispersion curves from 3.125 Hz to 9987.5 Hz. The analytical solution is calculated by an orthotropic model proposed in [31] for composite structures. Depending on the symmetry of the structure, the wavenumbers in the other directions can be obtained symmetrically from the estimated wavenumbers. Notably, AKSI-C is developed on the plane wave model. Thus, it can provide a reliable k-space of the tested honeycomb sandwich composite plate using the line-based displacements as input due to the fact that the wave field of the tested honeycomb sandwich plate presents a close-plane wave field/direct field in each direction due to the high damping properties. On this basis, 3D dispersion curves, as shown in Fig. 7(b), indicate that the dispersion curves of the honeycomb sandwich structure are characterized by θ-dependent and frequency-dependent properties. This property can be clearly seen from the profile of the 3D dispersion curves. Fig. 8 presents the k-space of this honeycomb sandwich structure at different frequencies, which illustrates the complex dynamic bending behavior of

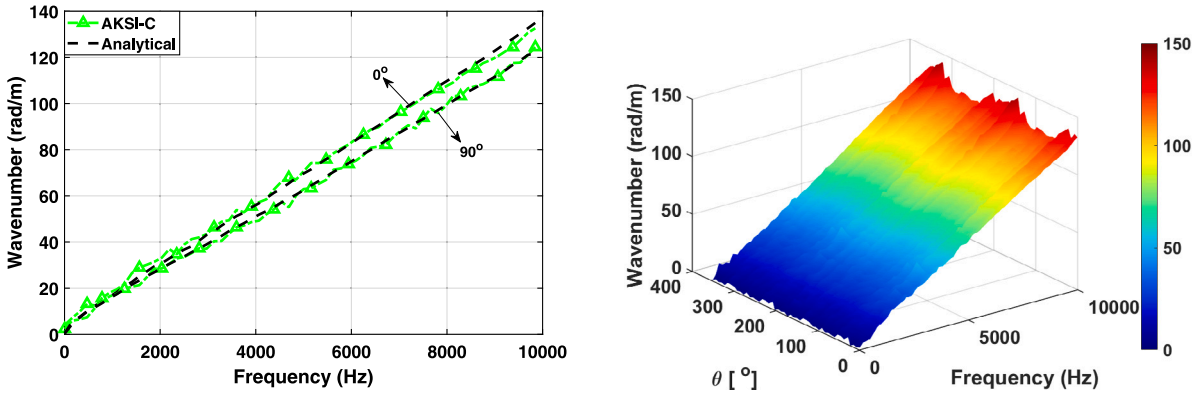

(a) (b)

Fig. 7. Identification of wave dispersion characteristics for the honeycomb sandwich composite structure via AKSI-C: (a) the dispersion curves in two principal directions; (b) 3D dispersion curves as a function of direction and frequency.

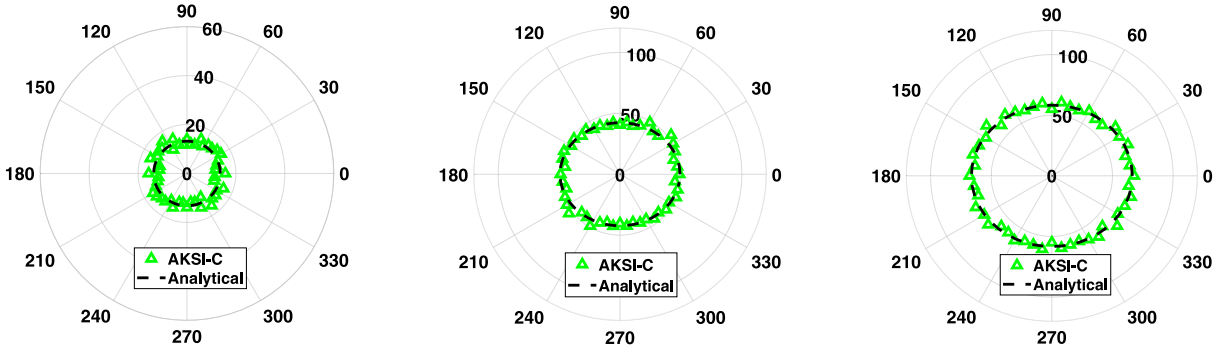

(a) (b) (c)

Fig. 8. Identification of k-space characteristics for the honeycomb sandwich composite structure via AKSI-C: (a) k-space at 784.375 Hz; (b) k-space at 3284.375 Hz; (c) k-space at 4690.625 Hz.

this structure. Specifically, the profiles of k-space vary from circular to elliptic in shape, which exhibits that the dynamic behavior of sandwich structure changes from isotropy in low frequency to orthotropy in high frequency within the frequency range tested in this work. The orthotropic property is more pronounced in higher frequencies with the more elliptic k-space profile. This k-space characteristic can be explained by the fact that in the low-frequency range, the motion of the sandwich is governed by the bending stiffness of skins, and the structure behaves as a classic isotropic plate, whereas, with frequency increase, the dynamic behavior of the sandwich is controlled by the out-of-plate shear effects and the shear stiffness of the honeycomb core becomes more and more dominant, leading to the transition of dynamic behavior from isotropy to orthotropy.

It is well known that in the sandwich structure, the transition frequency can describe the changes in structural dynamic behavior from the wave motion governed by the skin's bending stiffness to the one dominated by the core's shear stiffness. Most of the past work mainly focuses on the analytical analysis of transition frequency based on frequency-independence mechanical parameters from material tables obtained using static experiments. However, this is still a problem for accurate modeling and dynamic analysis due to the complexity of the mechanical properties of the honeycomb sandwich structure. For this reason, the transition frequency is estimated directly from the experimental dispersion curves extracted by AKSI-C, allowing us to obtain a transition frequency close to reality. The dispersion curves between 0° and 90° are plotted in Fig. 9. From this figure, three observations can be obtained: (i) from observing the intersection of dispersion curves in two principal directions, the transition frequency is estimated as 784.4 Hz, which is close to the analytical frequency transition (760.21 Hz) based on the corrected mechanical properties of this structure [43]. This can further validate that the estimated value in the presented work is reliable; (ii) in the frequency range lower than transition frequency, the wavenumbers do not differ dramatically in each direction, indicating that the honeycomb sandwich composite structure has an approximately isotropic dynamic behavior at low frequencies. Despite this, the wavenumbers at 0° (blue curve) are slightly smaller than those in other directions in the zoomed sub-picture. This is probably because the plate is governed by the bending stiffness of carbon fiber epoxy skins oriented at 0°, where wave propagation is the fastest; (iii) in the frequency range higher than the transition frequency within the frequency range tested in this work, the plate motion is more and more controlled by the shear stiffness of the honeycomb core. It is clear to see that the wavenumbers at 90° become the smallest, and the velocity becomes the biggest. This experiment result illustrates that the honeycomb core is stiffest at the direction of 90°, which has a good agreement with the fact that the equivalent shear stiffness G_{yz} is higher than G_{xz} provided by the Table 1. In addition, the wavenumbers near the 90° direction are significantly bigger than those near the 0° direction. This difference increases with frequency, demonstrating that the orthotropy of the honeycomb sandwich composite structure is more pronounced with frequency.

The dispersion surfaces of the real part of the wavenumber κ and the imaginary part of the wavenumber τ are presented in Fig. 10. The damping loss factor η is calculated by Eq. (26). The 3D damping loss factor, as shown in Fig. 11(b), illustrates that the tested honeycomb sandwich structure has a high damping effect and the damping loss factor can be a function of the wave propagating direction and frequency.

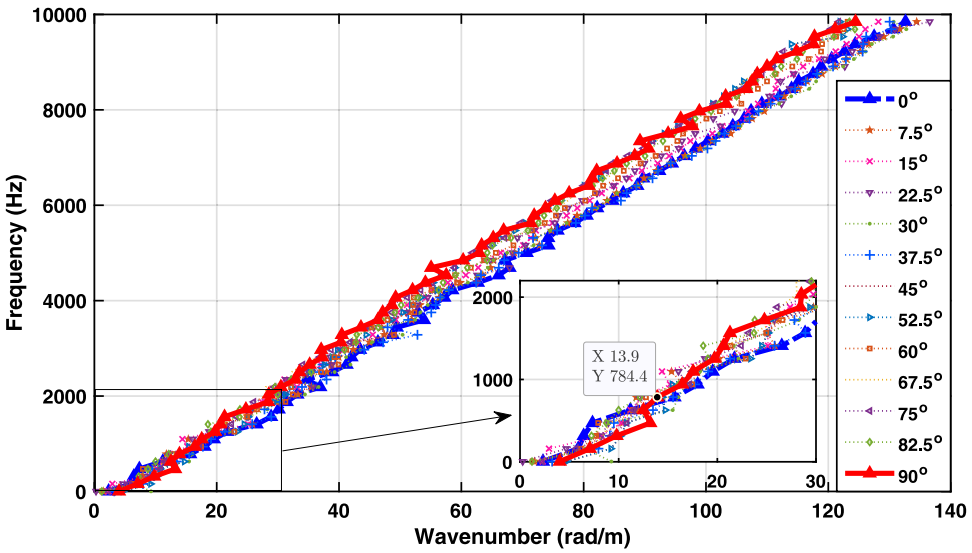

Fig. 9. Transition frequency estimation and the contribution of individual layer properties on the dynamic behavior of the honeycomb sandwich composite structure through experimental dispersion curves extracted by AKSI-C between 0° and 90°.

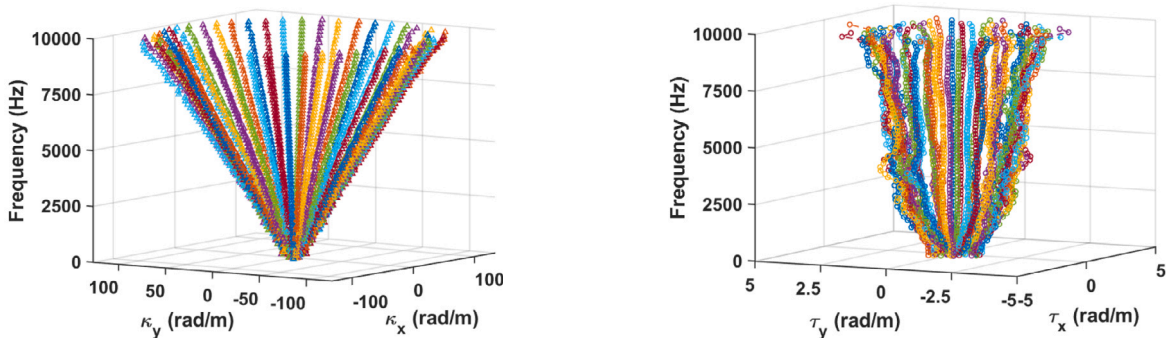

(a) (b)

Fig. 10. Discrete dispersion surfaces extracted by AKSI-C on the honeycomb sandwich composite structure: (a) real part κ; (b) imaginary part τ.

In addition, the displacement field at 5000 Hz, as shown in Fig. 11(a), presents a single emission from the excitation point outwards with few reflected waves due to the high damping properties.

The accuracy of the wave propagation characterization presented above depends on the fact that AKSI-C is a reliable inverse method in experimental conditions. The first advantage of the AKSI-C is that it is not limited to periodic sampling. To validate it, 40 non-periodic samples are randomly selected from the 59 periodic samples measured along the direction of 0° at 9846.875 Hz, as shown in Fig. 12(a). Then the selected non-periodic samples are used as input parameters of AKSI-C and IWC. The resulting dispersion curves are compared in Fig. 12(b), where AKSI-C has a good estimation over the whole frequency range, free from the periodic sampling limitation. In comparison, IWC can estimate the dispersion curve accurately in the middle and high-frequency range in this case, while it suffers from low frequencies due to the few wavelengths contained in the displacement.

In an experimental environment, samples are inevitably subject to various perturbations. As shown in Fig. 11(a), the perturbation is visible in the displacement field. Under this condition, the k-space comparison between the three inverse methods is presented in Fig. 13. From this figure, one can obtain three conclusions: (i) AKSI-C is robust to perturbations, providing smooth and accurate k-space. This advantage is due to the introduction of integration of signals; (ii) IWC suffers from low frequency, while with frequency increase, it shows good robustness against perturbations; (iii) INCOME is sensitive to perturbations due to the nature of limitation of the Prony method, affecting the assessment of the wave propagation characterization.

4.2. Locally resonant meta-structures: Experimental results and validation

In this study, the steel plate with and without resonators are tested. In the bare configuration, the coherence function calculated from all samples from the 2D grid is shown in Fig. 14(a). The coherence function value close to near zero indicates that the samples are heavily influenced by signal noise. Therefore, it can be seen that at frequencies higher than around 500 Hz, the plate was tested in the high-level signal noise condition. The resulting dispersion curves along the x direction obtained by IWC, INCOME, and AKSI-C are shown in Fig. 14(b), where the robustness of IWC and AKSI-C to signal noise can be validated again, providing a reliable estimation, while INCOME is not capable of extracting the accurate dispersion curve in this condition.

In the resonator configuration, the band gap existing in the dispersion curve along the x direction can be identified by the IWC and AKSI-C, as shown in Fig. 15(a). One can observe that the resonator frequency is tuned at 1284 Hz, generating a band gap with an approximate width of 187 Hz under the resonator configuration described in Section 3.2.2. Fig. 15(b) shows the Frequency Response Functions (FRFs) comparison in two configurations. In this figure, a significant drop in amplitude can be observed within the frequency range corresponding to the band gap, illustrating the ability of the meta-structure

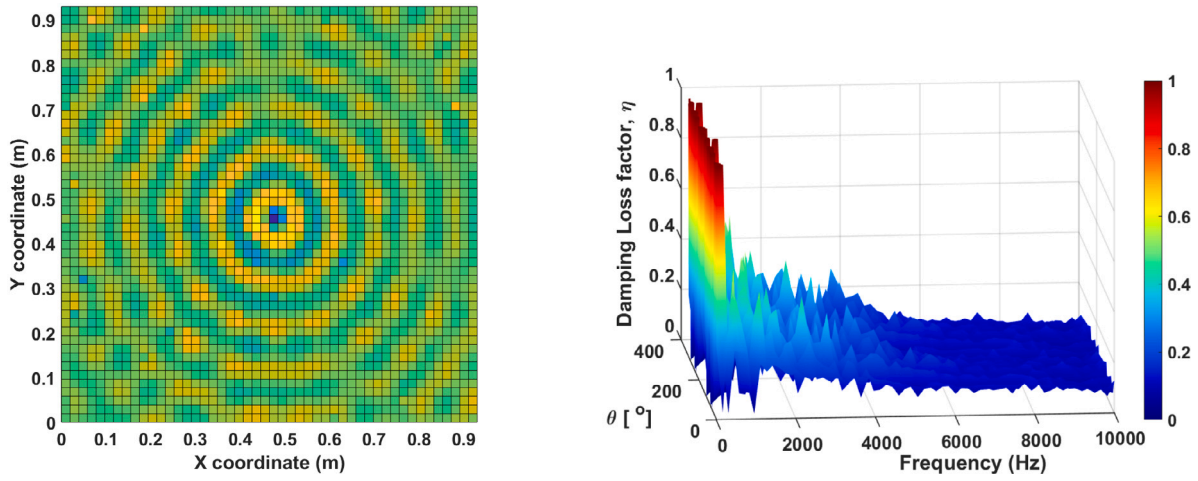

(a) (b)

Fig. 11. Characterization of the damping properties of the honeycomb sandwich composite structure: (a) displacement field at 5000 Hz; (b) 3D damping loss factor extracted by AKSI-C as a function of direction and frequency.

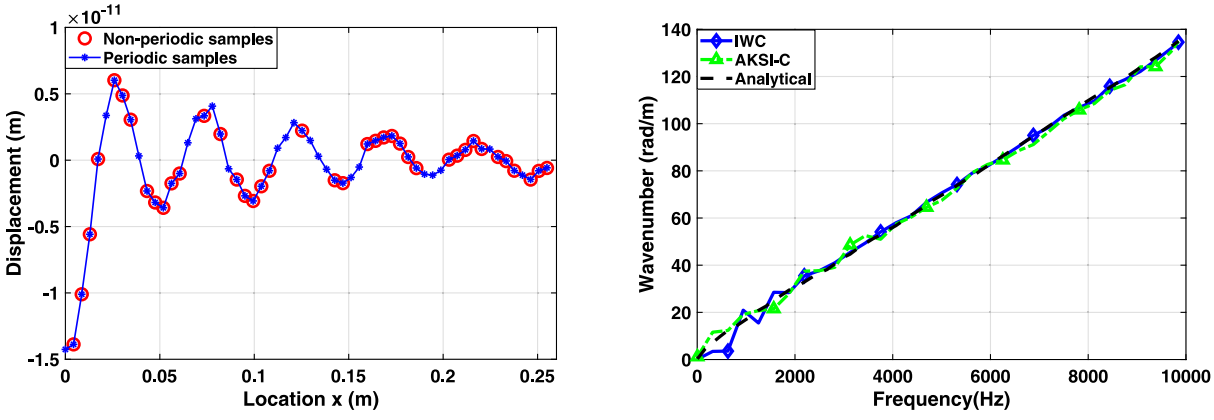

(a) (b)

Fig. 12. Dispersion curve comparison for the honeycomb sandwich composite structure under non-periodic sampling condition, extracted by AKSI-C and IWC: (a) operational deflection shape along 0° direction at 9846.875 Hz; (b) dispersion curves.

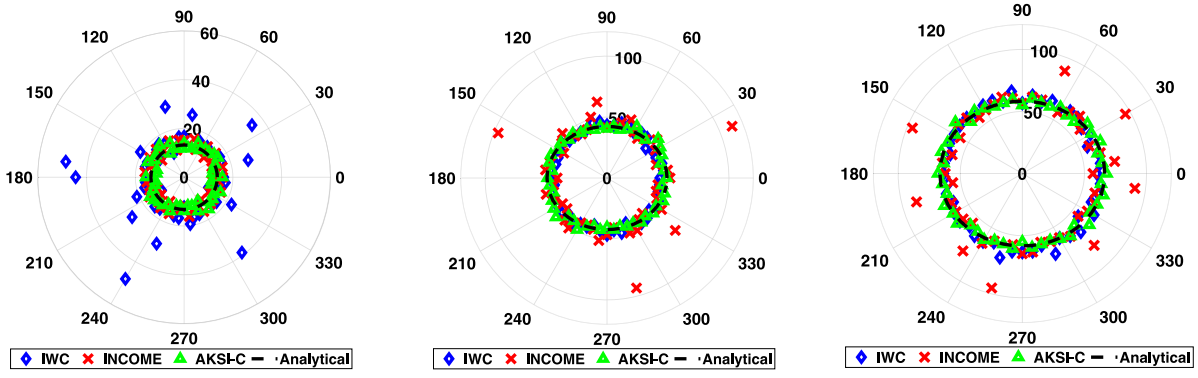

(a) (b) (c)

Fig. 13. K-space comparison for the honeycomb sandwich composite structure, extracted by AKSI-C, IWC and INCOME: (a) k-space at 784.375 Hz; (b) k-space at 3284.375 Hz; (c) k-space at 4690.625 Hz.

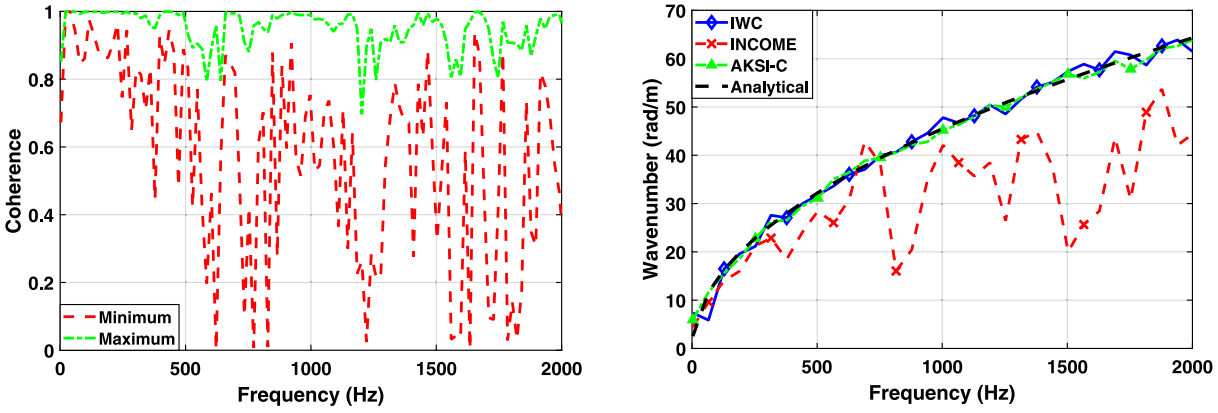

Fig. 14. Dispersion curve at the x direction comparison for the steel plate under high-level signal noise condition, extracted by AKSI-C, IWC, and INCOME: (a) coherence function; (b) dispersion curves along the x direction.

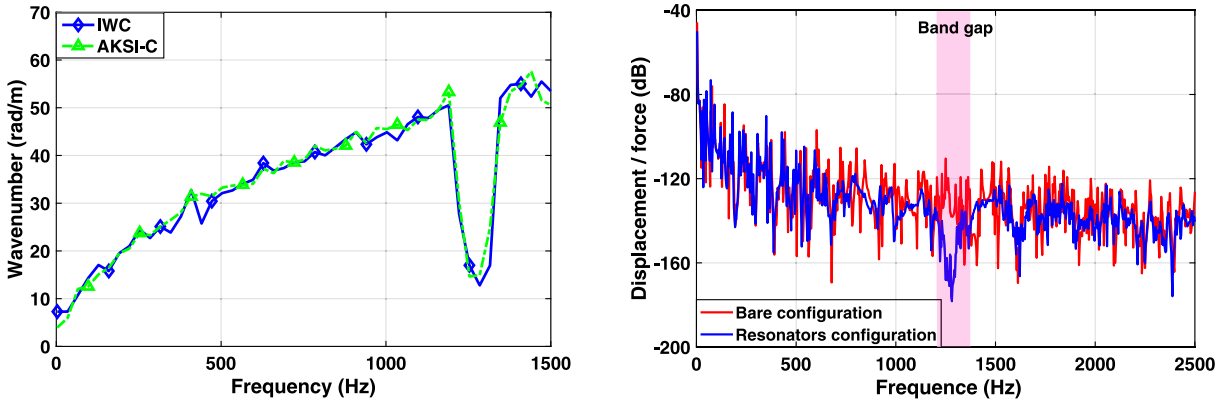

Fig. 15. The band gap identification for the locally resonant meta-structure: (a) dispersion curves at the x direction obtained by AKSI-C and IWC along the x direction; (b) FRF comparison for bare configuration and resonator configuration.

to control the wave attenuation in the structure. In addition, the effect of the local resonances-induced band gap on structural vibration reduction can also be obtained by the displacement field comparison in two configurations. For example, the resulting displacement fields comparison at 1300 Hz (a frequency within the band gap) are shown in Fig. 16. As shown in this figure, a lot of reflected waves are produced at the edges of the plate without resonators due to the low damping effect (see Fig. 16(a)). In contrast, the displacements decrease clearly with increasing distance from the excitation in the locally resonant meta-structure because of the energy dissipation within the band gap (see Fig. 16(b)).

4.3. Periodic rib-stiffened composite plates: Experimental results and validation

Firstly, the orthogonally ribbed plate is studied in this section. The finite element model of this plate is built using COMSOL. The numerical model is shown in Fig. 1, and the mechanical and geometric parameters are shown in Table 2. The boundary condition is chosen as the free-free boundary condition, and the boundary force is put along the top side of the structure. The solid element is used for modeling, and the degree of freedom is 637839. Finally, 30 periodic samples with a sampling interval of 1 cm are measured along the same line as the experimental test. The numerical and experimental dispersion curves identified by AKSI-C are presented in Fig. 17(b), where a good agreement between the extracted dispersion curves and the analytical dispersion curve can be observed. The analytical results are calculated through Eq. (27). Moreover, the singularity of the wavenumber occurs at around 275 Hz, producing a band gap with a width of about 89 Hz. This phenomenon results from the inner resonance of the internal plate. Specifically, the bending stiffness and thickness of the beam grids are much greater than that of the internal plate, causing the inhomogeneous dynamic behavior of these two parts and inducing the occurrence of the inner local resonance phenomenon. The displacement field at 281 Hz is shown in Fig. 17(a), indicating the reduction of structural vibration within the band gap. These results show the potential of the periodic rib-stiffened composite plate in designing the wave attenuation in the frequency band of interest.

Secondly, the uni-directionally ribbed plate is investigated. The dispersion curves extracted by AKSI-C and IWC for the uni-directionally ribbed plate without resonators are presented in Fig. 18(a). This figure shows that these two inverse methods enable to identify the band gap of ribbed plate and the band gap happens around 809 Hz. The inner mechanism is same as the orthogonally ribbed plate. The interesting work of this case is to add the resonators designed in Section 3.2.3 on the surface of the uni-directionally ribbed plate to adjust the band gap location. As expected, the resulting dispersion curves, as shown in Fig. 18(b), show a shift of resonance frequency towards the higher frequency, changing from 809 Hz to 1149.219 Hz. This phenomenon results from the mixed mechanism between the inner resonance of the internal plate and the local resonator-induced resonance.

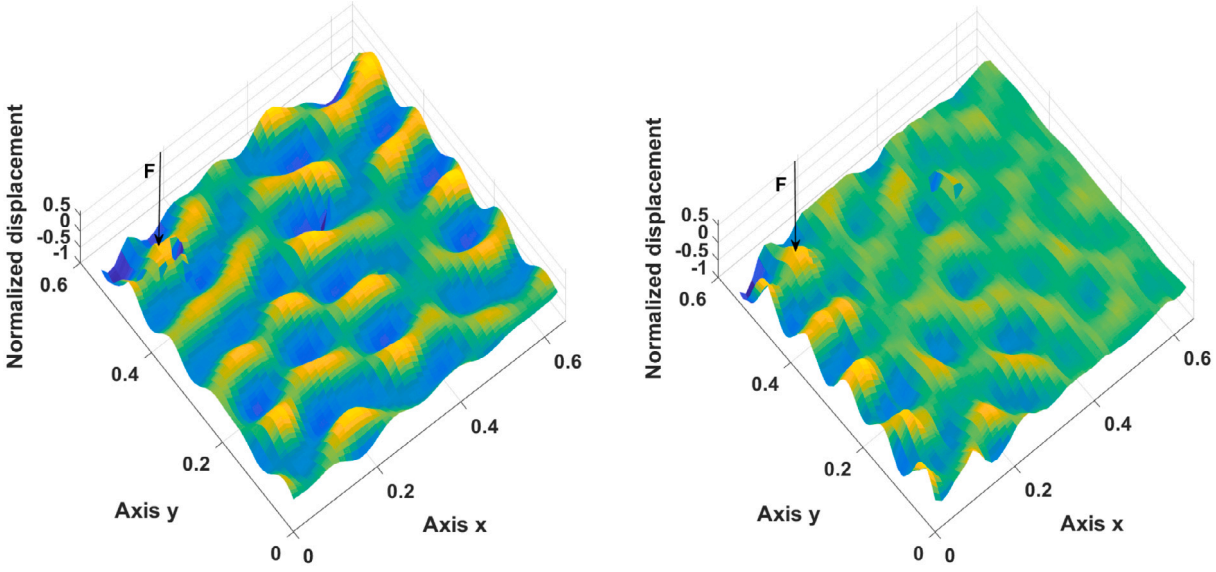

Fig. 16. Normalized displacement fields comparison of two configurations at 1300 Hz: (a) bare configuration; (b) resonator configuration.

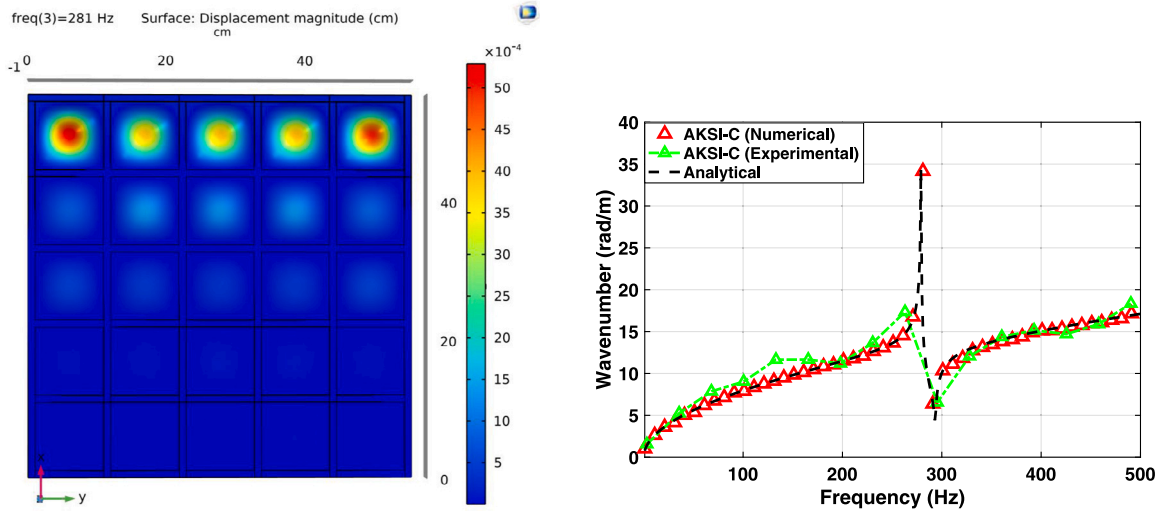

Fig. 17. Effect of inner resonance phenomenon of the orthogonally ribbed plate on wave propagation: (a) displacement field at 281 Hz for the numerical model; (b) the band gap identification with AKSI-C numerically and experimentally.

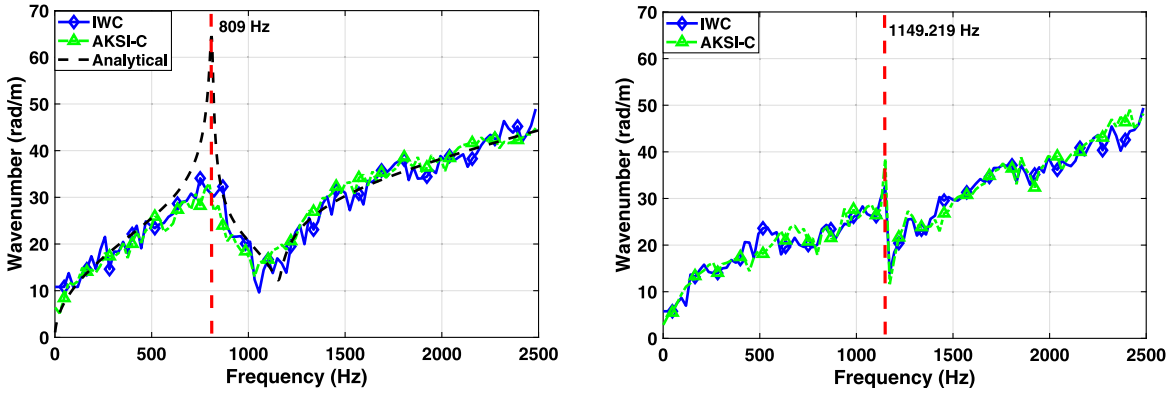

Fig. 18. Effect of the mixed-resonance-induced phenomenon of the uni-directionally ribbed plate on wave propagation: (a) dispersion curves extracted by AKSI-C and IWC for the uni-directionally ribbed plate without resonators; (b) dispersion curves extracted by AKSI-C and IWC for the uni-directionally ribbed plate with resonators.

The study of two periodic rib-stiffened composite plates demonstrates their remarkable wave propagation manipulation abilities, providing the possibility of reducing the structural vibration and controlling wave propagation by designing the resonator distributions and changing the relationship between the stiffeners and the internal plate.

5. Conclusions

This paper proposed the Algebraic K-Space Identification method in the Cartesian coordinate system (AKSI-C). The first step of this method is to build a new partial differential equation with two variables k_x and k_y in the wavenumber domain using multivariate Laplace transform. Then the partial differential equation is transformed into a regression formula with the integral of 2D signals in the spatial domain. Finally, the complex wavenumbers can be identified by the least squares method. The extracted complex wavenumbers are able to provide a lot of helpful information to describe structural dynamic behavior and characterize the wave propagation in the complex composite structures. Due to the advantages of AKSI-C being robust to signal noise and having low computational cost, it has been applied to provide a reliable and in-situ analysis for wave propagation characteristics in three complex composite structures only using the displacement field obtained from the non-destructive testing in the present work.

The honeycomb sandwich composite structure is first tested from 3.125 Hz to 9987.5 Hz. AKSI-C has a good performance on the k-space identification of the tested honeycomb sandwich composite plate using the line-based displacements as input. This is because that the wave field of the tested honeycomb sandwich plate presents a close-plane wave field/direct field in each direction due to the high damping properties, which is adapted to the signal model required for AKSI-C. The direction- and frequency-dependent properties of orthotropic dynamic behavior and damping loss factor are identified. The contribution of the individual layer to the overall dynamic behavior is explored using the estimated transition frequency, which is in good agreement with theoretical analysis. Then, active tuning of the flexural wave band gap is investigated in a locally resonant meta-structure. Finally, two periodic rib-stiffened composite plates are studied, including a unidirectionally ribbed plate and an orthogonally ribbed plate. This study explores the mechanism of the inner resonance phenomenon in such structures and opens the possibility of optimizing the performance of rib-stiffened composite plates on wave attenuation in specific frequency ranges.

From a practical application standpoint, the proposed method can be applied to characterize the structural wave propagation of multi-dimensional signals under complex conditions. Moreover, it holds the potential to solve inverse problems in the vibroacoustic field, including structural damage detection, mechanical parameter identification, and structural optimization. These promising capabilities are worth further investigation and exploration in future studies. so far, like other inverse methods such as INCOME, and IWC, AKSI-C uses plane wave signals as the input signals. From the development of the method point of view, a promising perspective is to introduce the non-plane wave model into the theory of AKSI-C. This adaptation aims to address structures with more complex wave fields, and it constitutes a key objective for the forthcoming development of AKSI-C.

The current version of AKSI-C is developed based on the plane wave model, which limits the applicability of AKSI-C to extract complex wavenumbers in all directions for structures with non-plane wave fields, such as the low-damping steel plates and ribbed plates. To the authors' understanding, this is still a challenge for most plane wave-based inverse methods, such as Prony and IWC. In the future, the optimization of AKSI-C built on the non-plane wave model is worth exploring for the more general structures. On the other hand, a promising direction is to investigate the application of AKSI-C for solving more vibroacoustic inverse problems, such as structural health monitoring or ultrasonic inspections of anisotropic materials via identifying steering angle, the multi-wave mode separation and coupling to study more complex structural dynamic behavior, and structural identification of complex composite structures. Moreover, in this work, the maximum frequency we tested was 10 kHz. The performance of AKSI-C at ultrasonic frequencies, beyond the scope of this work, deserves further investigation in the future.

CRediT authorship contribution statement

Xuefeng Li: Conceptualization, Methodology, Experiments, Validation, Formal analysis, Writing – original draft. **Mohamed Ichchou:** Conceptualization, Methodology, Supervision, Writing – review & editing. **Pascal Fossat:** Validation, Writing – review & editing. **Abdelmalek Zine:** Conceptualization, Methodology. **Noureddine Bouhaddi:** Conceptualization, Methodology.

Declaration of competing interest

The authors declare that they have no known competing financial interests or personal relationships that could have appeared to influence the work reported in this paper.

Data availability

No data was used for the research described in the article.

Acknowledgments

This work is supported by the LabEx CeLyA (Centre Lyonnais d'Acoustique, ANR-10-LABX-0060) of Université de Lyon. The research of X. Li is funded by the China Scholarship Council (CSC).

References

[1] Lim C, Yaw Z, Chen Z, et al. Periodic and aperiodic 3-D composite metastructures with ultrawide bandgap for vibration and noise control. Compos Struct 2022;287:115324. http://dx.doi.org/10.1016/j.compstruct.2022.115324.
[2] Peng X, Wang M, Yi B, Li J, Wu H, Jiang S. Optimization design of stacking sequence and material distribution for variable thickness hybrid composite structure based on improved stacking sequence table. Compos Struct 2023;307:116641. http://dx.doi.org/10.1016/j.compstruct.2022.116641.
[3] Zhang W, Li Z, Wang J, Scarpa F, Wang X. Mechanics of novel asymmetrical re-entrant metamaterials and metastructures. Compos Struct 2022;291:115604. http://dx.doi.org/10.1016/j.compstruct.2022.115604.
[4] Mizukami K, Kawaguchi T, Ogi K, Koga Y. Three-dimensional printing of locally resonant carbon-fiber composite metastructures for attenuation of broadband vibration. Compos Struct 2021;255:112949. http://dx.doi.org/10.1016/j.compstruct.2020.112949.
[5] Boutin C, Fossat P, Droz C, Ichchou M. Dynamics of ribbed plates with inner resonance: Analytical homogenized models and experimental validation. Eur J Mech A Solids 2020;79:103838. http://dx.doi.org/10.1016/j.euromechsol.2019.103838.
[6] Tufano G, Errico F, Robin O, Droz C, Ichchou M, Pluymers B, et al. K-space analysis of complex large-scale meta-structures using the inhomogeneous wave correlation method. Mech Syst Sig Process 2020;135:106407. http://dx.doi.org/10.1016/j.ymssp.2019.106407.
[7] Tang D, Zhang W, Li L, Ye X. Theoretical and experimental modeling of beam-type flexural wave behaviours of orthogonally stiffened plates. Int J Mech Sci 2021;198:106395. http://dx.doi.org/10.1016/j.ijmecsci.2021.106395.
[8] Cotoni V, Langley R, Shorter P. A statistical energy analysis subsystem formulation using finite element and periodic structure theory. J Sound Vib 2008;318(4–5):1077–108. http://dx.doi.org/10.1016/j.jsv.2008.04.058.
[9] Zhou C, Lainé J, Ichchou M, Zine A. Multi-scale modelling for two-dimensional periodic structures using a combined mode/wave based approach. Compos Struct 2015;154:145–62. http://dx.doi.org/10.1016/j.compstruc.2015.03.006.
[10] Yang Y, Mace BR, Kingan MJ. A wave and finite element based homogenised model for predicting sound transmission through honeycomb panels. J Sound Vib 2019;463:114963. http://dx.doi.org/10.1016/j.jsv.2019.114963.
[11] Yang Y, Mace BR, Kingan MJ. Vibroacoustic analysis of periodic structures using a wave and finite element method. J Sound Vib 2019;457:333–53. http://dx.doi.org/10.1016/j.jsv.2019.06.009.
[12] Nilsson E, Nilsson A. Prediction and measurement of some dynamic properties of sandwich structures with honeycomb and foam cores. J Sound Vib 2002;251(3):409–30. http://dx.doi.org/10.1006/jsvi.2001.4007.

[13] Ghinet S, Atalla N. Vibro-acoustic behaviors of flat sandwich composite panels. Trans Can Soc Mech Eng 2006;30(4):473–93. http://dx.doi.org/10.1139/tcsme-2006-0030.
[14] Chronopoulos D, Troclet B, Bareille O, Ichchou M. Modeling the response of composite panels by a dynamic stiffness approach. Compos Struct 2013;96:111–20. http://dx.doi.org/10.1016/j.compstruct.2012.08.047.
[15] Guillaumie L. Vibroacoustic flexural properties of symmetric honeycomb sandwich panels with composite faces. J Sound Vib 2015;343:71–103. http://dx.doi.org/10.1016/j.jsv.2014.12.026.
[16] Baho O, Zergoune Z, Ichchou M, Harras B, Benamar R, Troclet B, et al. On global bending–shear core transition effects for the vibroacoustic of sandwich structures: Analytical and numerical investigations. Compos Struct 2016;154:453–63. http://dx.doi.org/10.1016/j.compstruct.2016.07.062.
[17] Zhong Y, Shi Z, Luo Q, Zhang M. A simplified semi-analytical model for predicting the global and local responses of hybrid honeycomb-like sandwich panel. Thin-Walled Struct 2023;182:110307. http://dx.doi.org/10.1016/j.tws.2022.110307.
[18] Razgordanisharahi A, Ghassabi AA, Hellmich C. Free vibration analysis of cylindrical honeycomb sandwich panels using state-space Levy method. Thin-Walled Struct 2023;182:110308. http://dx.doi.org/10.1016/j.tws.2022.110308.
[19] Mcdaniel JG, Shepard WS. Estimation of structural wave numbers from spatially sparse response measurements. J Acoust Soc 2000;108(4):1674–82. http://dx.doi.org/10.1121/1.1310668.
[20] Berthaut J, Ichchou M, Jezequel L. K-space identification of apparent structural behaviour. J Sound Vib 2005;280(3–5):1125–31. http://dx.doi.org/10.1016/j.jsv.2004.02.044.
[21] Halkyard C. Maximum likelihood estimation of flexural wavenumbers in lightly damped plates. J Sound Vib 2007;300(1–2):217–40. http://dx.doi.org/10.1016/j.jsv.2006.08.019.
[22] Geslain A, Raetz S, Hiraiwa M, Abi Ghanem M, Wallen S, Khanolkar A, et al. Spatial Laplace transform for complex wavenumber recovery and its application to the analysis of attenuation in acoustic systems. J Appl Phys 2016;120(13):135107. http://dx.doi.org/10.1063/1.4963827.
[23] Margerit P, Lebée A, Caron J-F, Boutillon X. High resolution wavenumber analysis (HRWA) for the mechanical characterisation of viscoelastic beams. J Sound Vib 2018;433:198–211. http://dx.doi.org/10.1016/j.jsv.2018.06.062.
[24] Margerit P, Lebée A, Caron J-F, Ege K, Boutillon X. The high-resolution wavevector analysis for the characterization of the dynamic response of composite plates. J Sound Vib 2019;458:177–96. http://dx.doi.org/10.1016/j.jsv.2019.06.026.
[25] Boukadia RF, Claeys C, Droz C, Ichchou M, Desmet W, Deckers E. An inverse convolution method for wavenumber extraction (INCOME): Formulations and applications. J Sound Vib 2022;520:116586. http://dx.doi.org/10.1016/j.jsv.2021.116586.
[26] Ribeiro L, Dal Poggetto V, Huallpa B, Arruda J. Bloch wavenumber identification of periodic structures using Prony's method. Mech Syst Sig Process 2022;178:109242. http://dx.doi.org/10.1016/j.ymssp.2022.109242.
[27] Claeys CC, Vergote K, Sas P, Desmet W. On the potential of tuned resonators to obtain low-frequency vibrational stop bands in periodic panels. J Sound Vib 2013;332(6):1418–36. http://dx.doi.org/10.1016/j.jsv.2012.09.047.
[28] Claeys CC, Sas P, Desmet W. On the acoustic radiation efficiency of local resonance based stop band materials. J Sound Vib 2014;333(14):3203–13. http://dx.doi.org/10.1016/j.jsv.2014.03.019.
[29] Van Nimmen K, Lombaert G, De Roeck G, Van den Broeck P. The impact of vertical human-structure interaction on the response of footbridges to pedestrian excitation. J Sound Vib 2017;402:104–21. http://dx.doi.org/10.1016/j.jsv.2017.05.017.
[30] Ichchou M, Berthaut J, Collet M. Multi-mode wave propagation in ribbed plates: Part I, wavenumber-space characteristics. Int J Solids Struct 2008;45(5):1179–95. http://dx.doi.org/10.1016/j.ijsolstr.2007.09.032.
[31] Ichchou M, Bareille O, Berthaut J. Identification of effective sandwich structural properties via an inverse wave approach. Eng Struct 2008;30(10):2591–604. http://dx.doi.org/10.1016/j.engstruct.2008.02.009.
[32] Malatesta MM, Moll J, Kudela P, Radzieński M, De Marchi L. Wavefield analysis tools for wavenumber and velocities extraction in polar coordinates. IEEE Trans Ultrason Ferroelectr Freq 2021;69(1):399–410. http://dx.doi.org/10.1109/TUFFC.2021.3106040.
[33] Chang C, Yuan F. Extraction of guided wave dispersion curve in isotropic and anisotropic materials by matrix pencil method. Ultrasonics 2018;89:143–54. http://dx.doi.org/10.1016/j.ultras.2018.05.003.
[34] Morandi F, Robin O, Barbaresi L, Garai M, Atalla N, Quaegebeur N, et al. Benchmarking of methods for the identification of flexural wavenumbers in wooden plates. Universitätsbibliothek der RWTH Aachen; 2019, http://dx.doi.org/10.18154/RWTH-CONV-239092.
[35] Roozen N, Labelle L, Leclere Q, Ege K, Alvarado S. Non-contact experimental assessment of apparent dynamic stiffness of constrained-layer damping sandwich plates in a broad frequency range using a Nd: YAG pump laser and a laser Doppler vibrometer. J Sound Vib 2017;395:90–101. http://dx.doi.org/10.1016/j.jsv.2017.02.012.
[36] Li X, Ichchou M, Zine A, Droz C, Bouhaddi N. An algebraic wavenumber identification (AWI) technique under stochastic conditions. Mech Syst Sig Process 2023;188:109983. http://dx.doi.org/10.1016/j.ymssp.2022.109983.
[37] Fliess M, Sira-Ramirez H. An algebraic framework for linear identification. ESAIM Control Optim Calc Var 2003;9:151–68. http://dx.doi.org/10.1051/cocv:2003008.
[38] McDaniel JG, Dupont P, Salvino L. A wave approach to estimating frequency-dependent damping under transient loading. J Sound Vib 2000;231(2):433–49. http://dx.doi.org/10.1006/jsvi.1999.2723.
[39] Rak M, Ichchou M, Holnicki-Szulc J. Identification of structural loss factor from spatially distributed measurements on beams with viscoelastic layer. J Sound Vib 2008;310(4–5):801–11. http://dx.doi.org/10.1016/j.jsv.2007.11.026.
[40] Mariani A, Giorgetti A, Chiani M. Model order selection based on information theoretic criteria: Design of the penalty. IEEE Trans Signal Process 2015;63(11):2779–89. http://dx.doi.org/10.48550/arXiv.1910.03980.
[41] Badeau R, David B, Richard G. Selecting the modeling order for the ESPRIT high resolution method: An alternative approach. In: 2004 IEEE international conference on acoustics, speech, and signal processing. Vol. 2. IEEE; 2004, p. ii–1025. http://dx.doi.org/10.1109/ICASSP.2004.1326435.
[42] Okumura S, Nguyen V-H, Taki H, Haïat G, Naili S, Sato T. Rapid high-resolution wavenumber extraction from ultrasonic guided waves using adaptive array signal processing. Appl Sci 2018;8(4):652. http://dx.doi.org/10.3390/app8040652.
[43] Zergoune Z. Meso-macro approach for modeling the acoustic transmission through sandwich panels [Ph.D. thesis], Lyon; 2016.
[44] Droz C, Robin O, Ichchou M, Atalla N. Improving sound transmission loss at ring frequency of a curved panel using tunable 3D-printed small-scale resonators. J Acoust Soc Am 2019;145(1):EL72–8. http://dx.doi.org/10.1121/1.5088036.